Supplementary Information

Recurring summer and winter droughts from 4.2-3.97 thousand years ago in north India

Alena Giesche[a*], David A. Hodell[a], Cameron A. Petrie[b], Gerald H. Haug[c], Jess F. Adkins[d], Birgit Plessen[e], Norbert Marwan[f], Harold J. Bradbury[ag], Adam Hartland[h], Amanda D. French[h], Sebastian F. M. Breitenbach[i]

[a] Godwin Laboratory for Palaeoclimate Research, Department of Earth Sciences, University of Cambridge, Cambridge CB2 3EQ, United Kingdom
[b] Department of Archaeology, University of Cambridge, Cambridge CB2 3DZ, United Kingdom
[c] Climate Geochemistry Department, Max Planck Institute for Chemistry, Mainz 55020, Germany
[d] Division of Geological and Planetary Sciences, California Institute of Technology, Pasadena, CA 91125, USA
[e] Section Climate Dynamics and Landscape Evolution, Helmholtz Centre Potsdam, German Research Centre for Geosciences GFZ, Potsdam 14473, Germany
[f] Potsdam Institute for Climate Impact Research (PIK), Potsdam 14473, Germany
[g] Department of Earth, Ocean, and Atmospheric Sciences, University of British Columbia, Vancouver, BC, Canada
[h] Environmental Research Institute, School of Science, Faculty of Science and Engineering, University of Waikato, Hamilton 3216, New Zealand
[i] Department of Geography and Environmental Sciences, Northumbria University, Newcastle upon Tyne NE1 8ST, UK

* To whom correspondence should be addressed.
Corresponding Author: Alena Giesche, Department of Earth Sciences, Cambridge CB2 3EQ, UK
Email: alena.giesche@gmail.com

This file includes:

Supplementary Discussion

Dharamjali Cave study site

Dharamjali Cave (29°31'28.9" N, 80°12'28.0" E) is located at 2162 m a.s.l. near Deodar village in the lesser Himalayas in Uttarakhand state, northern India. The cave is developed within the Middle Proterozoic (1300-1200 Ma) Sor Formation, which includes underlying Sor Slate (interbedded slates and shales with argillaceous and dolomitic limestone) and the overlying Thalkedar Limestone (finely laminated dolomitic limestone), occasionally intruded by basic igneous rocks (Nautiyal, 1990). The area above the cave is dominated by C_3-type vegetation (with a lower $\delta^{13}C$ signature compared to C_4-type), composed of dense forest including mainly oaks (*Quercus incana*), *Rhododendron*, and *Pinus roxburghii* along with smaller shrubs and herbs on top of a relatively thin (20-30 cm) soil cover (Sanwal et al., 2013).

The cave is 30 m long, made up of two main chambers, with one narrow entrance at its highest point (Supplementary Fig. S10) (Sanwal et al., 2013). In winter, the cave's geometry promotes replacement of warmer air inside the cave with denser cold outside air, which enhances ventilation and CO_2 exchange with the atmosphere. Conversely, in summer, the narrow entrance and downward passage orientation supports formation of a cold-air lake (cold, dense air accumulates in the cave) that suppresses ventilation, with ventilation then limited to cold summer nights. Tectonics are active in this region, and Dharamjali Cave has been previously investigated as a recorder of seismic events, because it contains tilted stalagmites with regrowth on different axes, as well as evidence for multiple ceiling collapses (Rajendran et al., 2016).

Based on data collected in 2009, relative humidity in Dharamjali Cave ranges between 50 and 70%, and temperature ranges from 8 to 15°C (Sanwal et al., 2013), supporting the notion of active ventilation. Rainfall from GPCC data (Meyer-Christoffer et al., 2018) shows that rainfall at this location averages 225 mm during the winter half of the year (Nov-Apr), compared to 1475 mm in the summer half (May-Oct) (Supplementary Fig. S3). The cave is actively dripping throughout the year, though maximum infiltration occurs during the summer season with drip rates of 20-30 drops/min compared to 3-8 drops/min in the winter (Sanwal et al., 2013). The cave therefore is highly sensitive and responsive to seasonal changes in precipitation amounts. Today's average winter monsoon precipitation at the cave location, c. 10% of the annual total, barely exceeds potential evapotranspiration during the winter months.

Based on the Online Isotopes in Precipitation Calculator (OIPC) v3.2 model database (Bowen and Revenaugh, 2003), the average summer (Jun-Sep) rainfall, weighted by monthly precipitation amount, has a $\delta^{18}O$ value of -9.1‰, a δD value of -60.2‰, and d-excess of 12.3‰, distinct from the rest of the year (Oct-May), also weighted by amount, with $\delta^{18}O$ = -7.5‰, δD = -48.4‰, and d-excess = 11.6‰ (Supplementary Fig. S2). Published modern Dharamjali Cave dripwater $\delta^{18}O$ ranges between -6.5‰ and -5.5‰ (Sanwal et al., 2013), which may reflect sampling during spring months or evaporation along the flow path. However, dripwater data collected by our team in 2006 ranges between -9.5‰ in July and -8.6‰ in October, which matches unevaporated precipitation. Because the amount of rainfall in just the four months of June-September (c. 1300 mm) vastly exceeds the rest of the year (<400 mm), and the rainfall from these four months has significantly lower $\delta^{18}O$ and δD values, the average annual water isotope composition would be skewed towards more negative ISM values. A relatively stronger or longer summer monsoon would consequently also result in more negative $\delta^{18}O$ / δD, and vice versa. Finally, evaporation should be relatively weaker during the ISM season, and cave temperatures are warmer, both resulting in more negative rain- and dripwater $\delta^{18}O$ and δD values. This mixed annual rainfall composition and changes in cave conditions would be incorporated by any speleothem growing in this location. Since the residence time of the water in the epikarst is quite short, growth layers in a speleothem might also reflect distinct seasonal changes, including summer and winter rainfall $\delta^{18}O$. However, modern potential evapotranspiration is higher than precipitation for all winter months except January and February, resulting in minimal effective contribution of winter rainfall to the dripwater signal under today's conditions.

Climate and tectonics affecting stalagmite growth in Dharamjali Cave

Previously studied Dharamjali Cave speleothems include DH-1, DH-3 and DH-4 (Rajendran et al., 2016; Kotlia et al., 2018). In this study, DHAR-1 shows a change in calcite to aragonite mineralogy just before 4.2 ka BP that corresponds to a shift in growth axis around 4.2 ka BP in sample DH-4 (Rajendran et al., 2016). Possibly, the onset of drier conditions during the mid-late Holocene transition rerouted water in Dharamjali Cave and led to the growth of DHAR-1. During the 1100-year period after 4.2 ka BP, no growth axis shifts occur in DHAR-1 (or in any of the other previously studied stalagmites from Dharamjali Cave), and trace elements and carbon and oxygen stable isotopes likely serve as tectonically-unperturbed climate proxies. After 3.1 ka BP, tectonic disturbances may have occurred: in DHAR-1, two growth axis shifts occur at 3.1 ka BP and 2.78 ka BP, and a distinct break is visible just after 2.55 ka BP. In the DH-3 sample, a growth axis shift at 2.78 ka BP and a break at 2.5 ka BP were also attributed to tectonic events (Rajendran et al., 2016).

Carbon isotopes and cave ventilation dynamics

Speleothem $\delta^{13}C$ can be influenced by multiple factors, including vegetation composition and activity, soil microbial activity, organic carbon content in the soil and epikarst, soil temperature, host carbonate rock $\delta^{13}C$, prior carbonate/aragonite precipitation (and thus local effective moisture regime), and CO_2 degassing in epikarst and cave (e.g., Fohlmeister et al., 2020). The latter is further influenced by cave air pCO_2 level and cave ventilation, with lower pCO_2 levels and stronger ventilation fostering CO2 degassing and kinetic fractionation. All the factors act with varying relative importance at a given cave, and force the $\delta^{13}C$ signal in the same direction (higher $\delta^{13}C$ values under drier conditions, except soil respiration). The $\delta^{13}C$ proxy is complex and its main driver possibly changes throughout the record. Overall, we favor the option that PAP drives $\delta^{13}C$ from 4.2 to 3.97 ka BP when drought is the most severe, and that a combination of shifts in soil carbon via vegetation, ventilation, and CO_2 degassing (all primarily related to winter precipitation and/or temperature) drive the proxy thereafter.

Below, we expand on how cave ventilation might affect the $\delta^{13}C$ values. One notable result was that $\delta^{13}C$ did not perfectly match the $\delta^{44}Ca$ proxy, which is thought to exclusively reflect PAP (e.g., Owen et al., 2016; Magiera et al., 2019; de Wet et al., 2021). So, PAP does not seem to be the primary driver for $\delta^{13}C$, at least after 3.97 ka BP. The $\delta^{13}C$ proxy could still reflect a long-term soil carbon shift if we assume that the PAP driver passes a threshold and causes an abrupt change in the baseline $\delta^{13}C$ values after 3.97 ka BP. Alternatively, an increase in cave ventilation due to a change in season length could explain the divergence in $\delta^{13}C$ from $\delta^{18}O$ and $\delta^{44}Ca$. If the dry winter/cold season is longer and ventilation is favored in winter, then proportionally more aragonite (with correspondingly higher $\delta^{13}C$) could form during the colder months. Winter dripwater would either stem from the epikarst that is still saturated from summer monsoon rainfall late into the fall (i.e., a scenario where the summer monsoon is both stronger but also more seasonally compressed into a shorter span of months), or the dripwater represents directly infiltrating winter precipitation (which has a more positive $\delta^{18}O$ signature than summer precipitation at Dharamjali Cave, Supplementary Fig. S2a). In both cases, active CO_2 degassing in a highly ventilated cave environment would promote both higher $\delta^{13}C$ (and $\delta^{18}O$). However, between 3.97 and 3.4 ka BP there is a trend towards decreasing $\delta^{18}O$ while $\delta^{13}C$ increases. This suggests that the $\delta^{18}O$ signal may in fact be dampened or muted - with summer monsoon being comparatively so strong (lower $\delta^{18}O$) that even increased winter ventilation is not able to compensate (without a more intense summer monsoon, DHAR-1 would show an increase in $\delta^{18}O$). One caveat for the ventilation interpretation is that a longer dry winter season is not the only option; in fact, simply colder winter temperatures or longer winters (even with more wintertime precipitation) could also lead to an increase in $\delta^{13}C$. The independent drip rate proxies (transition metals Ni/Ca, Zn/Ca, and Cu/Ca), however, may shed some light on distinguishing these possibilities. Indeed, the transition metals indicate a slower drip rate around 3.6 ka BP (Fig. 2A) that would support the interpretation of $\delta^{13}C$ related to winter aridity rather than simply cooler temperatures. Since the drip rate proxies could reflect either summer or winter precipitation, the $\delta^{18}O$ (ISM proxy) becomes a useful tool for distinguishing when drip rate changes reflect winter versus summer rainfall.

At Dharamjali Cave, the ventilation situation is understood as outlined here: the site experiences a pronounced wet ISM season between June and September, and a dry season during the rest of the year (225 mm winter precipitation is observed from Nov-Apr) (Kotlia et al. 2018, Sanwal et al. 2013) (Supplementary Fig. S2). Effective infiltration (precipitation minus runoff and evapotranspiration) is confined largely to the ISM season (Supplementary Fig. S2a). At the same time, surface air temperature varies significantly on a seasonal scale (Supplementary Fig. S2b), with highest temperatures recorded in the summer. The cave itself opens on the shoulder of a narrow valley and is a single downward-oriented passage (ca. 28 degree slope) (Supplementary Fig. S11) that forms a cul de sac after ca. 50 m or so. This geometry has important bearings on the ventilation regime of the cave.

Observations (this study, and Sanwal et al., 2013) show that drips are active year-round, with ca. 20-30 drips/minute during the ISM season, and 3-8 drips/minute during the dry season. This drip behavior suggests a rapid response to infiltration events, with a short (though not quantified) lag period. The ventilation regime of the cave has not been monitored in detail, but given its geometry and local temperature conditions four scenarios can be deduced (Supplementary Fig. S11).

A. Summertime day ventilation (Supplementary Fig. S11a)
   During summer (and ISM season) the daytime surface air temperature is higher than inside the cave. Together with the cave's geometry this results in the formation of a cold air lake that keeps cool air in the cave. This situation hinders active ventilation of the cave, and allows accumulation of CO_2 (which is also brought in with active drips). Thus, high pCO_2 levels are expected during the wet summer season during the day. Under these conditions (high pCO_2 levels and reduced cave/surface air exchange) it is likely that both overall CO_2 degassing and kinetic fractionation of carbon isotopes (i.e., preferential degassing of ^{12}C from dripwater into cave air) is suppressed. $\delta^{13}C$ in speleothem carbonate growing in this scenario would be relatively negative (little enrichment).

B. Summertime night ventilation (Supplementary Fig. S11b)
During summer (and ISM season) the nighttime surface air temperature is likely still higher than inside the cave, although the difference between surface and cave air temperature (ΔT) would be lower. This would result in the retention of the cold air lake in the cave and/or partial ventilation by replacement of cool cave air with slightly colder surface air (if nighttime air cools sufficiently). This situation allows some limited ventilation of the cave and possibly some removal of CO_2 (brought in with active drips). Thus, pCO_2 levels are expected to be either stagnant or lower slightly during ISM season nights. Under these conditions (constant or lowering p CO_2 levels and limited cave/surface air exchange) it is likely that both overall CO_2 degassing and kinetic fractionation of carbon isotopes are limited, but at times active. $\delta^{13}C$ in speleothem carbonate growing in this scenario would likely remain relatively negative, or possibly slightly enriched.

C. Wintertime day ventilation (Supplementary Fig. S11c)
During the dry winter season the situation changes significantly at the cave site. Daytime outside temperatures are colder and ΔT would be low, such that sometimes the cave would be warmer, and sometimes colder than the surface air. This would allow for some exhaling of the cave (if cave air is warmer) and removal of cave air CO_2. The drip rates are lower compared to the summer and less CO_2 is transported with dripwater into the cave. Combining the lower CO_2 supply and somewhat limited ventilation would allow for only limited CO_2 degassing and isotope fractionation. This would result in speleothem $\delta^{13}C$ values being mid-ranging (not too kinetically enriched).

D. Wintertime night ventilation (Supplementary Fig. S11d)
During the dry winter nights cave air would be significantly warmer than the surface air, which would result in rigorous exhaling of the warm (rising) cave air and inflow of cold surface air (i.e., strong ventilation). Since the drip rates are low (Sanwal et al. 2013) during the dry season, under these conditions prolonged CO_2 degassing from incoming drips (which hang longer on the soda straws/stalactites) combines with fast removal of CO_2 from the cave and therefore active kinetic fractionation. This means that $\delta^{13}C$ in speleothems would be enriched.

Considering these four scenarios, it is unlikely that active ventilation would frequently fall together with times of high drip rates. Importantly (considering the sampling resolution achievable in the stalagmite) we argue that $\delta^{13}C$ is lower during the ISM season and higher during the winter season (we cannot resolve night/daytime differences in the stalagmites).

Whether more carbonate is deposited during the dry or the wet season remains speculative, due to a lack of monitoring. However, there are no longterm shifts in growth rate of the speleothem between 4.2 and 3.1 ka BP, and faster accumulation occurs only after 3.1 ka BP (Supplementary Fig. S4). With stronger ventilation during the dry season, one could expect to observe faster saturation of the incoming dripwater and thus faster growth. Alternatively, the growth during the ISM season might outpace the dry season deposition due to higher drip rates and loading of dripwater with dissolved inorganic carbon. This can only be resolved with seasonal monitoring of the cave.

Transition metals as a drip rate proxy

Transition metals such as zinc, copper, cobalt, and nickel have received increasing attention because of their tendency to bind to organic ligands (Hartland et al., 2014; Hartland and Zitoun, 2018). These elements have predicted and empirically derived distribution coefficients >1 in calcite (Lindeman et al., 2022), and this prediction also holds for aragonite although experimental research is still largely lacking (Wang and Xu, 2001; Fairchild and Baker, 2012). Because the elements Zn^{2+}, Cu^{2+}, Co^{2+} and Ni^{2+} all have Dx >1, increased prior calcite and aragonite precipitation during arid conditions would effectively remove a higher proportion of these components from dripwater and result in relatively lower X/Ca ratios in the speleothem. However, because of the ligand-binding characteristic of transition metals, the X/Ca ratio in the speleothem is also controlled by the length of time that the water film resides on the speleothem (Hartland and Zitoun, 2018). A lower drip rate with longer residence time on the speleothem allows for increased dissociation of the metals from the ligands. This means that higher X/Ca ratios can be found in the speleothem under more arid conditions, despite the occurrence of PCP or PAP and a transition metal D_x >1. The relative importance of this process is still being investigated (Höpker et al., 2021), and robust D_x values are still lacking for aragonite speleothems. Nevertheless, the PCA of trace elements in DHAR-1 (Fig. 3) suggests that some transition metals (e.g., Cu^{2+}, Ni^{2+}, and Zn^{2+}) may be a useful proxy of drip rate in aragonite stalagmites.

Supplementary References for Discussion

1. Nautiyal, A. C. Microfacies microfossils (organic-walled) in Middle Proterozoic Tejam Group of Kumaun Lesser Himalaya and paleoenvironmental significance. *J. Palaeontol. Soc. India*, **35**, 177-187 (1990).
2. Sanwal, J. et al. Climatic variability in Central Indian Himalaya during the last~ 1800 years: Evidence from a high resolution speleothem record. *Quat. Int.*, **304**, 183-192 (2013).
3. Rajendran, C. P. et al. Stalagmite growth perturbations from the Kumaun Himalaya as potential earthquake recorders. *J. Seismol.*, **20**, 579-594 (2016).
4. Meyer-Christoffer, A., Becker, A., Finger, P., Schneider, U., Ziese, M. Data from "GPCC Climatology Version 2018 at 0.25°: Monthly Land-Surface Precipitation Climatology for Every Month and the Total Year from Rain-Gauges built on GTS-based and Historical Data." GPCC at DWD. Available at https://doi.org/10.5676/DWD_GPCC/CLIM_M_V2018_025, Deposited 2018.
5. Bowen, G. J., Revenaugh, J. Interpolating the isotopic composition of modern meteoric precipitation. *Water Resour. Res.*, **39**, (2003).
6. Kotlia, B. S., Singh, A. K., Joshi, L. M., Bisht, K. Precipitation variability over Northwest Himalaya from ~4.0 to 1.9 ka BP with likely impact on civilization in the foreland areas. *J. Asian Earth Sci.*, **162**, 148-159 (2018).
7. Fohlmeister, J. Main controls on the stable carbon isotope composition of speleothems. *Geochim. Cosmochim. Acta*, **279**, 67-87 (2020).
8. Magiera, M. et al. Local and regional Indian Summer Monsoon precipitation dynamics during Termination II and the Last Interglacial. *Geophys. Res. Lett.*, **46**, 12454-12463 (2019).
9. Owen, R. A. et al. Calcium isotopes in caves as a proxy for aridity: Modern calibration and application to the 8.2 kyr event. *Earth Planet. Sci. Lett.*, **443**, 129-138 (2016).
10. Rawal, R. S., Pangtey, Y. P. S. Distribution and phenology of climbers of Kumaun in Central Himalaya, India. *Vegetatio*, **97**, 77-87 (1991).
11. de Wet, C. B. et al. Semiquantitative Estimates of Rainfall Variability During the 8.2 kyr Event in California Using Speleothem Calcium Isotope Ratios. *Geophys. Res. Lett.,* **48**, e2020GL089154, (2021).
12. Hartland, A., Fairchild, I. J., Müller, W., Dominguez-Villar, D. Preservation of NOM–metal complexes in a modern hyperalkaline stalagmite: Implications for speleothem trace element geochemistry. *Geochim. Cosmochim. Acta*, **128**, 29-43 (2014).
13. Hartland A., Zitoun, R. Transition metal availability to speleothems controlled by organic binding ligands. *Geochem. Perspect. Lett.* **8**, 22-25 (2018).
14. Lindeman, I., Hansen, M., Scholz, D., Breitenbach, S.F.M., Hartland, A. Effects of organic matter complexation on partitioning of transition metals into calcite: cave-analogue crystal growth experiments. *Geochim. Cosmochim. Acta*, **317**, 118-137 (2022).
15. Wang, Y., Xu, H. Prediction of trace metal partitioning between minerals and aqueous solutions: A linear free energy correlation approach. *Geochim. Cosmochim. Acta* **65**, 1529-1543 (2001).
16. Fairchild, I. J., Baker, A. Speleothem Science: From Process to Past Environments. Wiley, Hoboken, UK (2012).
17. Höpker, S. et al. Partitioning of trace metals in cave (and cave-analogue) carbonate precipitates – towards a quantitative hydrological proxy in stalagmites. *EGU General Assembly Conference Abstracts*, EGU21-13057 (2021).

Supplementary Figures

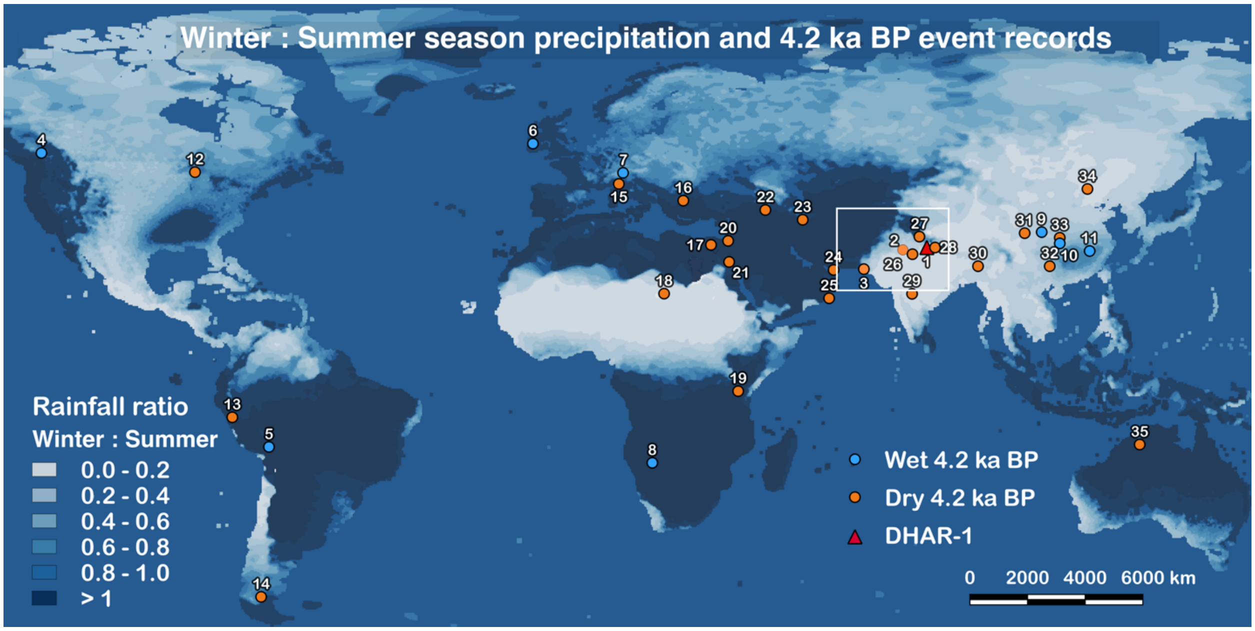

Fig. S1. Global map of the proportion of winter:summer precipitation. Global overview, including a box encompassing the close-up of the Indus region, and reconstructions for a dry (orange) and wet (blue) climate at 4.2 ka BP (numbered records are listed in Table S1). Contour lines represent the ratio of IWM (Nov–Apr) to ISM (May–Oct) precipitation based on the 0.25° GPCC v2018 dataset from 1951–2000 rain gauge data (Meyer-Christoffer et al., 2018).

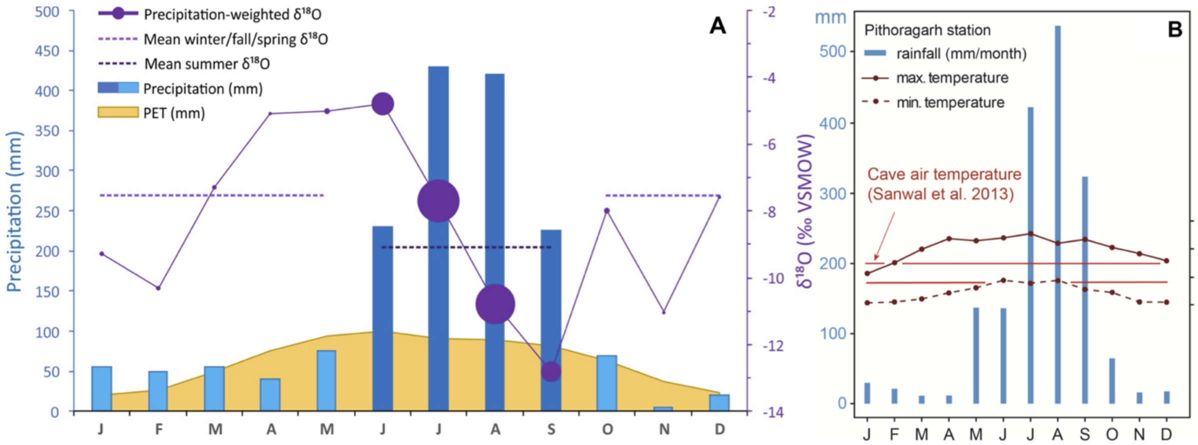

Fig. S2. Dharamjali Cave climate with modern monthly precipitation (blue bars) **(a)** from the 0.25° GPCC v2018 dataset from 1951-2000 rain gauge data (Meyer-Christoffer et al., 2018), shown with OIPC model-based monthly $\delta^{18}O$ values (purple circles) (Bowen and Revenaugh, 2003) where circle size denotes the weighting based on monthly precipitation amount. The average weighted $\delta^{18}O$ of summer months between June and September (dark purple dashed line) is compared to the average weighted $\delta^{18}O$ during the rest of the year between October and May (light purple dashed line). The yellow shading indicates monthly potential evapotranspiration, calculated using the Thornthwaite method (Palmer and Havens, 1958). In **(b)**, monthly rainfall, minimum and maximum temperatures from Pithoragarh (1981-1985) (dark red), modified after Rawal and Pangtey (1991), and cave air temperature (min & max) (light red) observed by Sanwal et al. (2013). The cave air is colder than surface air between roughly March and November, and warmer between November and the end of February. This suggests that for most of the year, the cave acts as a cold air trap.

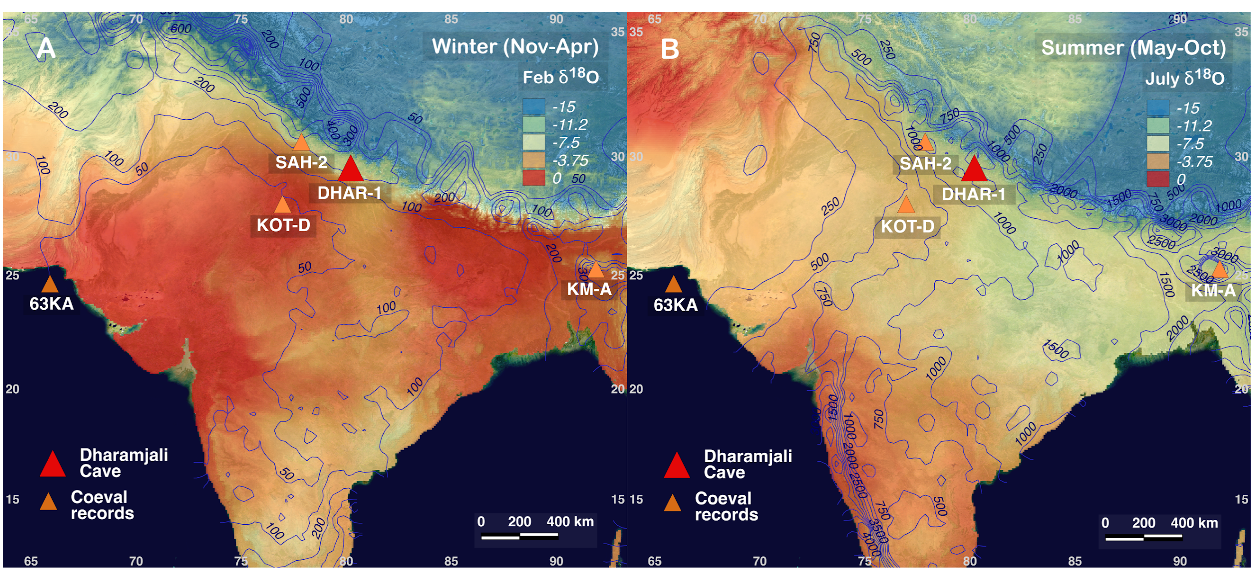

Fig. S3. Map of $\delta^{18}O$ of precipitation over India and surrounding regions, with rainfall contours. Shading denotes $\delta^{18}O_{precip}$ values for winter (February) and summer (July), respectively, from the OIPC model (Bowen and Revenaugh, 2003). Contours show winter (Nov-Apr) **(a)** and summer (May-Oct) **(b)** precipitation from the 0.25° GPCC v2018 dataset from 1951-2000 rain gauge data (Meyer-Christoffer et al., 2018). The location of Dharamjali Cave (this study, red triangle) is shown with other nearby records (orange triangles) including marine core 63KA (Giesche et al., 2019), Sahiya Cave stalagmite SAH-2 (Kathayat et al., 2017), Kotla Dahar Lake KOT-D (Dixit et al., 2014), and Mawmluh Cave stalagmite KM-A (Berkelhammer et al., 2012).

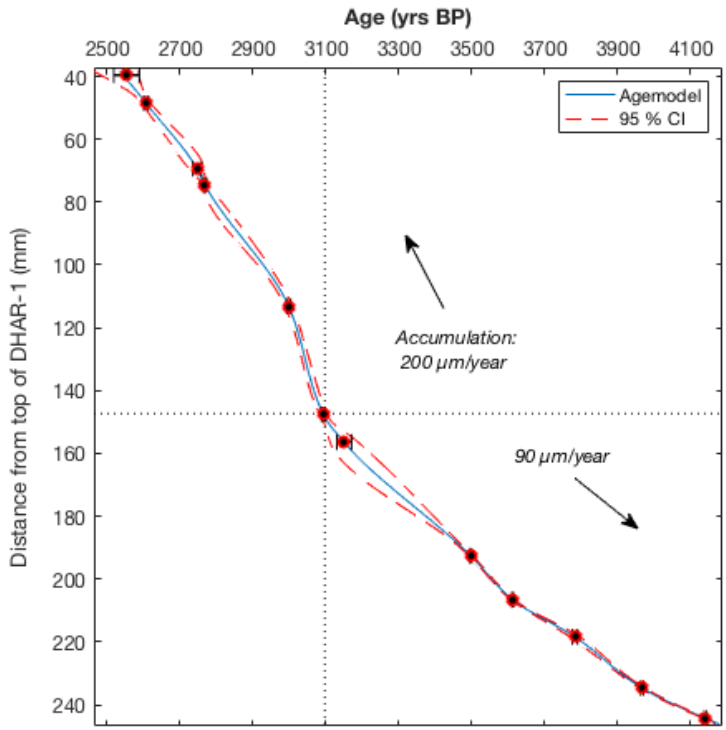

Fig. S4. DHAR-1 mean depth-age model (blue) with 95% confidence limits (red) based on COPRA (Breitenbach et al., 2012). Individual ages are plotted as circles with ±2σ error bars. Stalagmite mean growth rate is 90 µm/year where age is >3.1 ka BP and 200 µm/year where age is <3.1 ka BP.

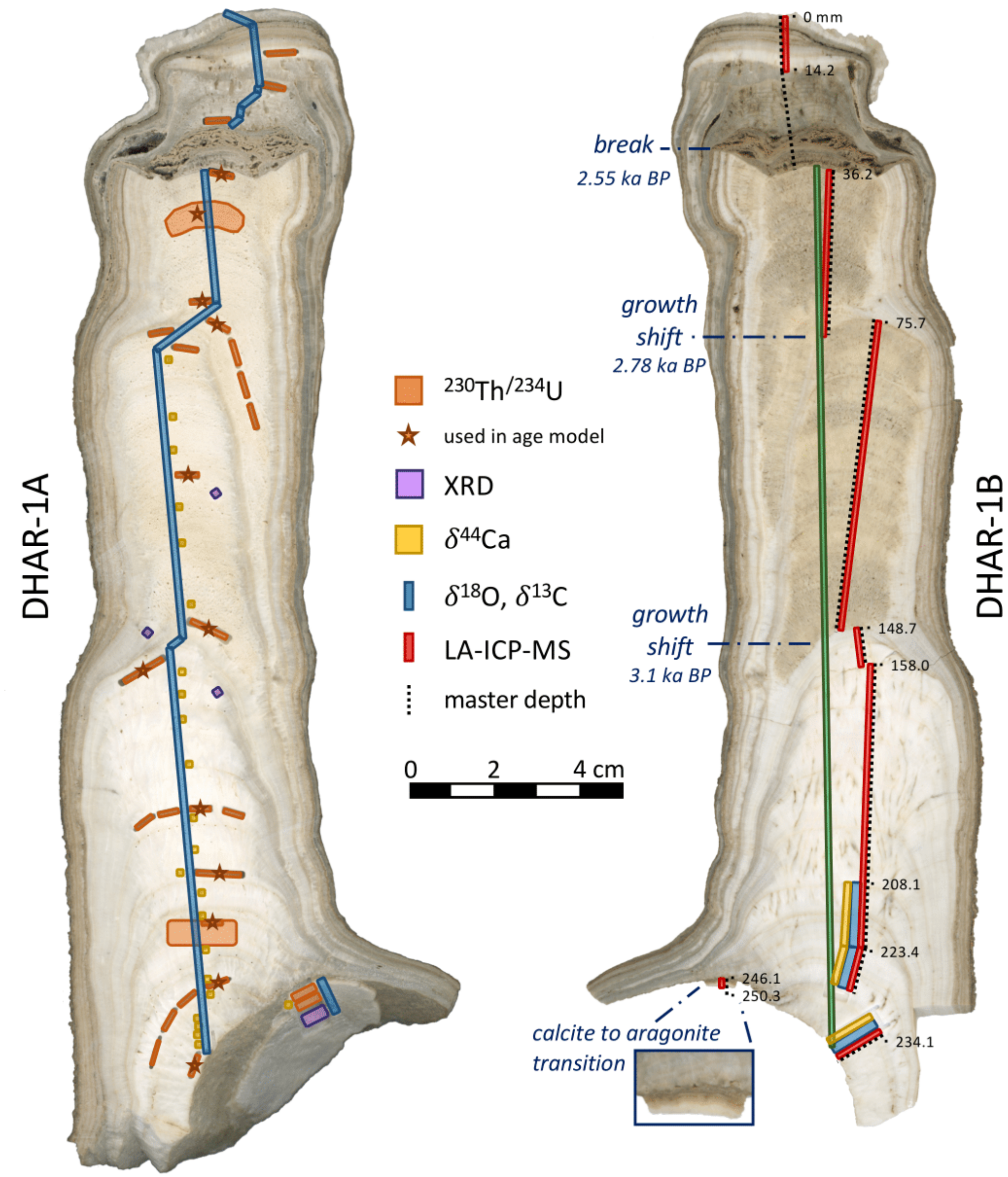

Fig. S5. Overview of analyses done on DHAR-1A and DHAR-1B halves of the DHAR-1 speleothem, showing sampling for $^{232}Th/^{234}U$ dates, XRD, low- and high-resolution $\delta^{13}C$ and $\delta^{18}O$, $\delta^{44}Ca$, and LA-ICP-MS. The master depth scale (mm), shown with critical transition depths, is delineated by a dotted black line.

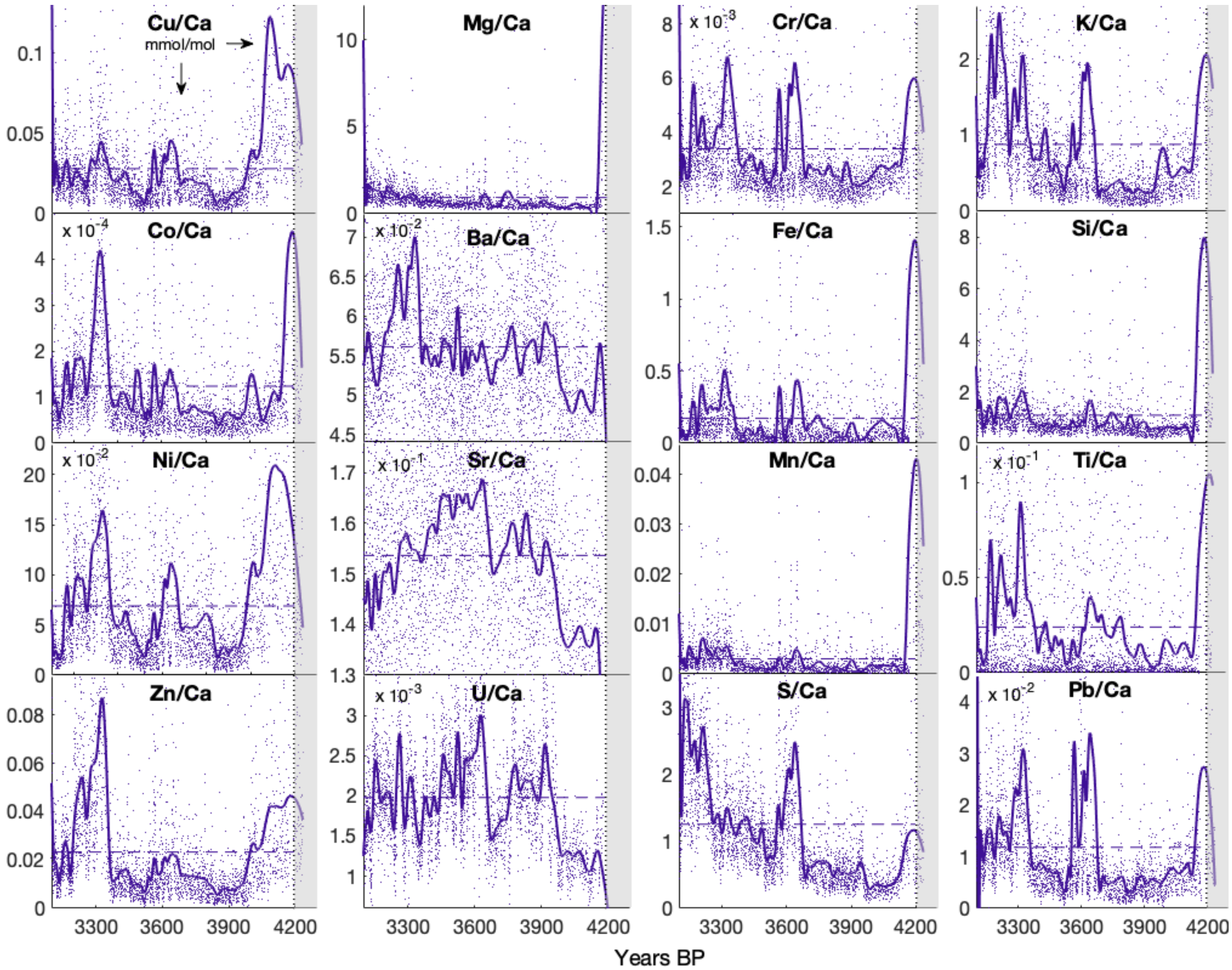

Fig. S6. LA-ICP-MS data (mmol/mol) for DHAR-1 from 4.2-3.1 ka BP, where horizontal dashed lines show the mean value of each series, grey vertical bars separate calcite (pre-4.2 ka BP) from aragonite (post-4.2 ka BP), and bold lines represent a 60-year LOESS smoothing. In the calcite base, Mg/Ca > 20-40 mmol/mol, Sr/Ca < 0.05 mmol/mol, U/Ca < $2*10^{-4}$ mmol/mol, and Ba/Ca < 0.03 mmol/mol (several transitions exceed the y-axis scale shown here).

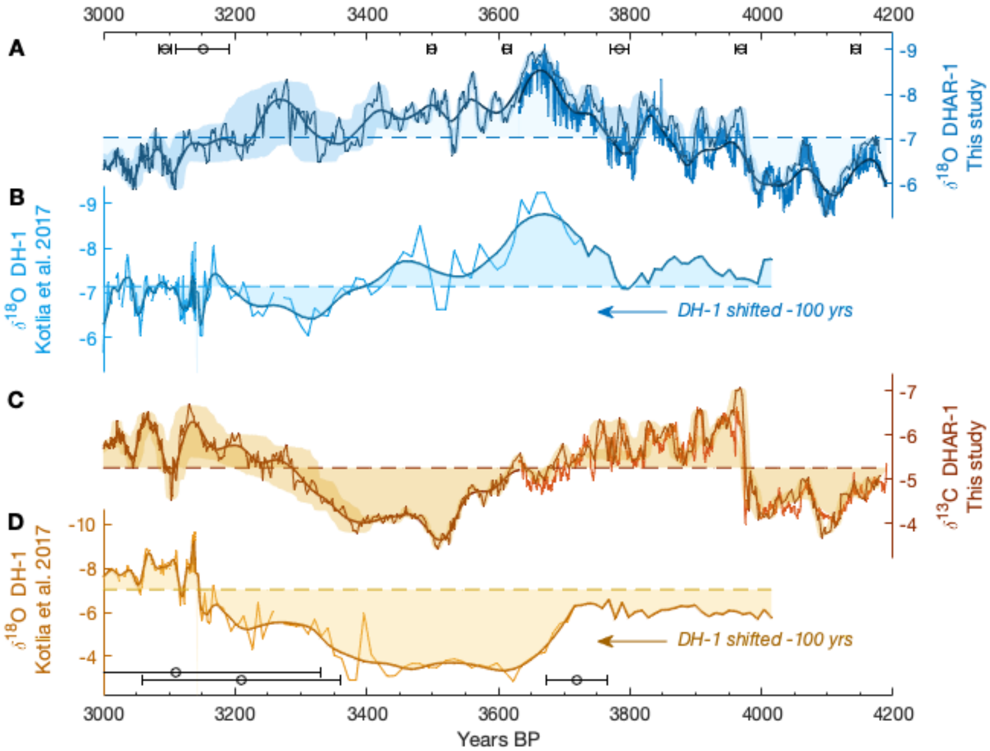

Fig. S7. Replication test for the two Dharamjali Cave stalagmite records DHAR-1 and DH-1 (Kotlia et al., 2018). The $\delta^{18}O$ (‰ VPDB, blue) and $\delta^{13}C$ (‰ VPDB, orange) time series over 4.2-3.0 ka BP for DHAR-1 (**a**, **c**, this study) and DH-1 (**b**, **d**, Kotlia et al., 2018). The DH-1 record (Kotlia et al., 2018) is shifted by 100 years younger (within the 2σ error of the dates) to best align with the age model proposed by this study. For the DHAR-1 series, shaded envelopes represent the 2.5 and 97.5% proxy confidence intervals. Horizontal dashed lines show the mean value of each series and bold lines represent a 100-year LOESS smoothing. U-series dates with $\pm 2\sigma$ error bars are shown near the upper (DHAR-1) and lower (DH-1) x-axes.

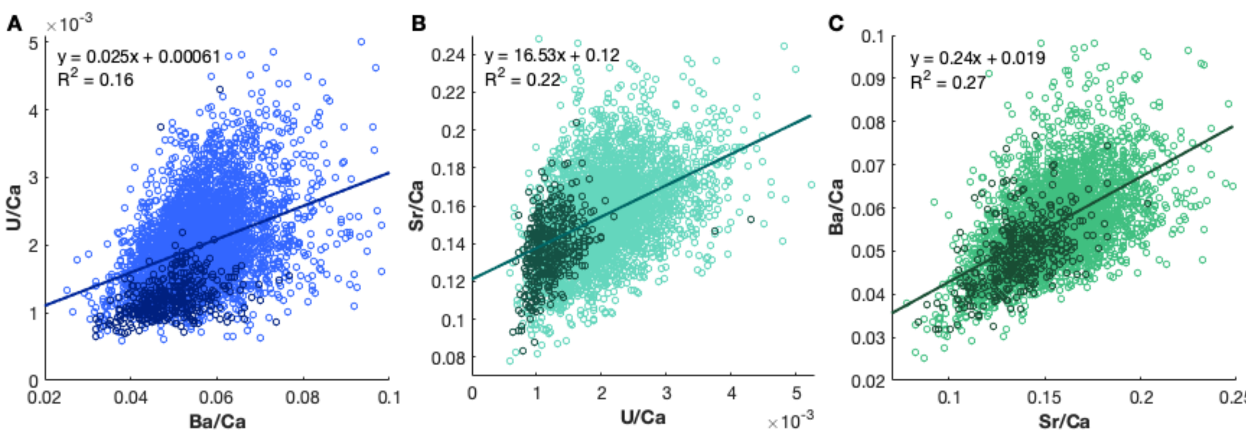

Fig. S8. Positive relationships between **(a)** U/Ca (mmol/mol), **(b)** Sr/Ca (mmol/mol), and **(c)** Ba/Ca (mmol/mol) from 4.2 to 3.1 ka BP, with darker points representing 4.2-3.98 ka BP. The unique distribution coefficients ($D_x = X/Ca_{Solid} / X/Ca_{Solution}$) in aragonite of $D_{Ba(Ar)} = 0.91 \pm 0.88$, $D_{Mg(Ar)} = 0.000097 \pm 0.00009$, $D_{Sr(Ar)} = 1.38 \pm 0.53$, and $D_{U(Ar)} = 6.26 \pm 4.54$ (Wassenburg et al., 2016), mean that U and Sr are sensitive indicators of PAP in aragonite speleothems. Another study found a lower but more precise value of DU(Ar) = 3.74 ± 1.13 (Jamieson et al., 2016). With more PAP, U ($D_{U(Ar)} > 1$) and Sr ($D_{Sr(Ar)} > 1$) are expected to decrease in the resulting speleothem. In the same scenario, Mg would be expected to increase ($D_{Mg(Ar)} < 1$); however, the low distribution coefficient means that other processes are quite likely to overprint such a signal (Wassenburg et al., 2016).

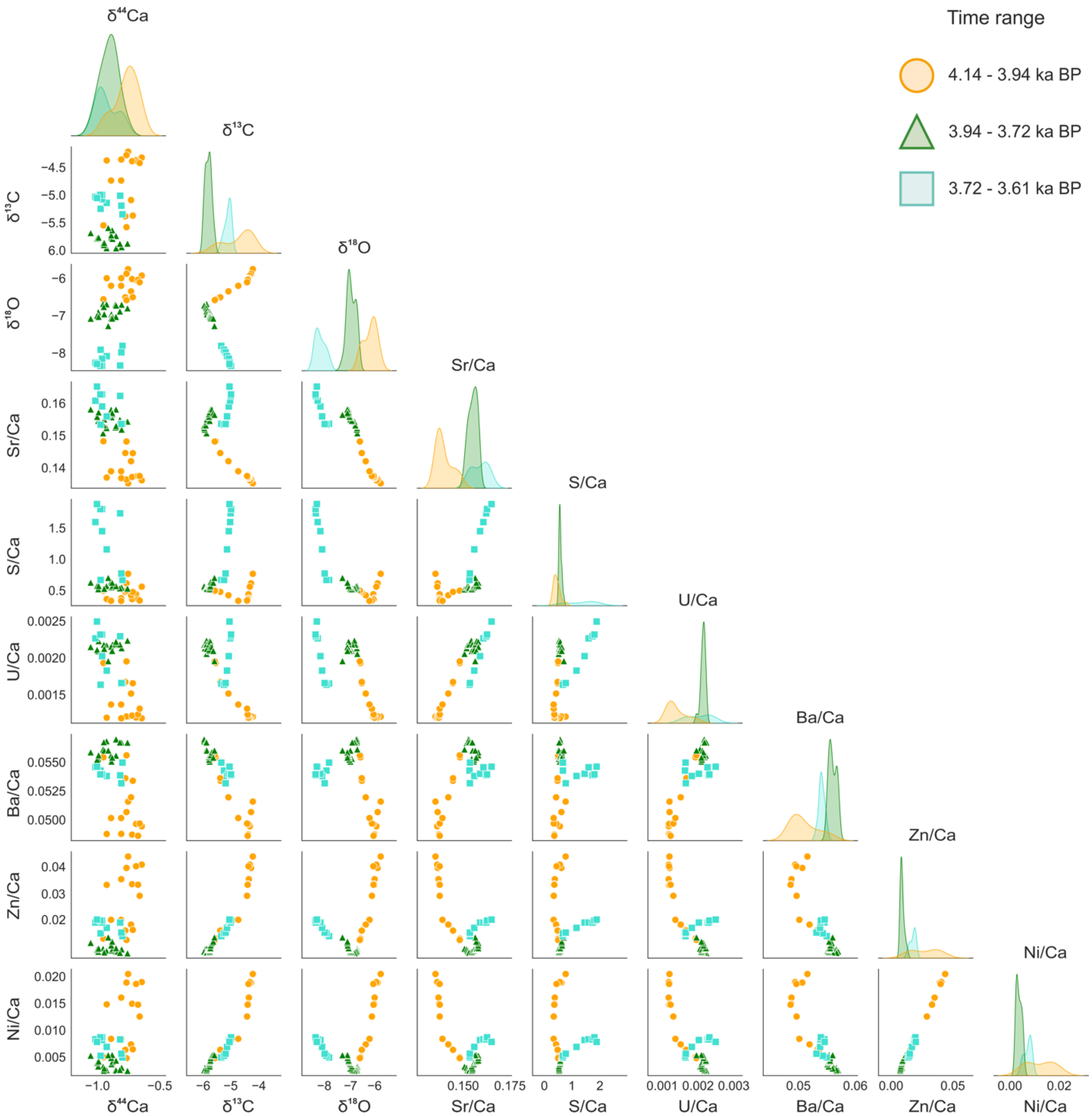

Fig. S9. Correlation matrix for isotope and trace element data (mmol/mol) split into three time periods of peak aridity (4.14-3.94 ka BP, orange circles), recovery of rainfall (3.94-3.72 ka BP, green triangles), and peak ISM recovery (3.72-3.63 ka BP, blue squares). Data distributions for each of the time periods are illustrated at the tops of the columns. Data were down-sampled to match $\delta^{44}Ca$ (‰ NIST), the lowest resolution proxy.

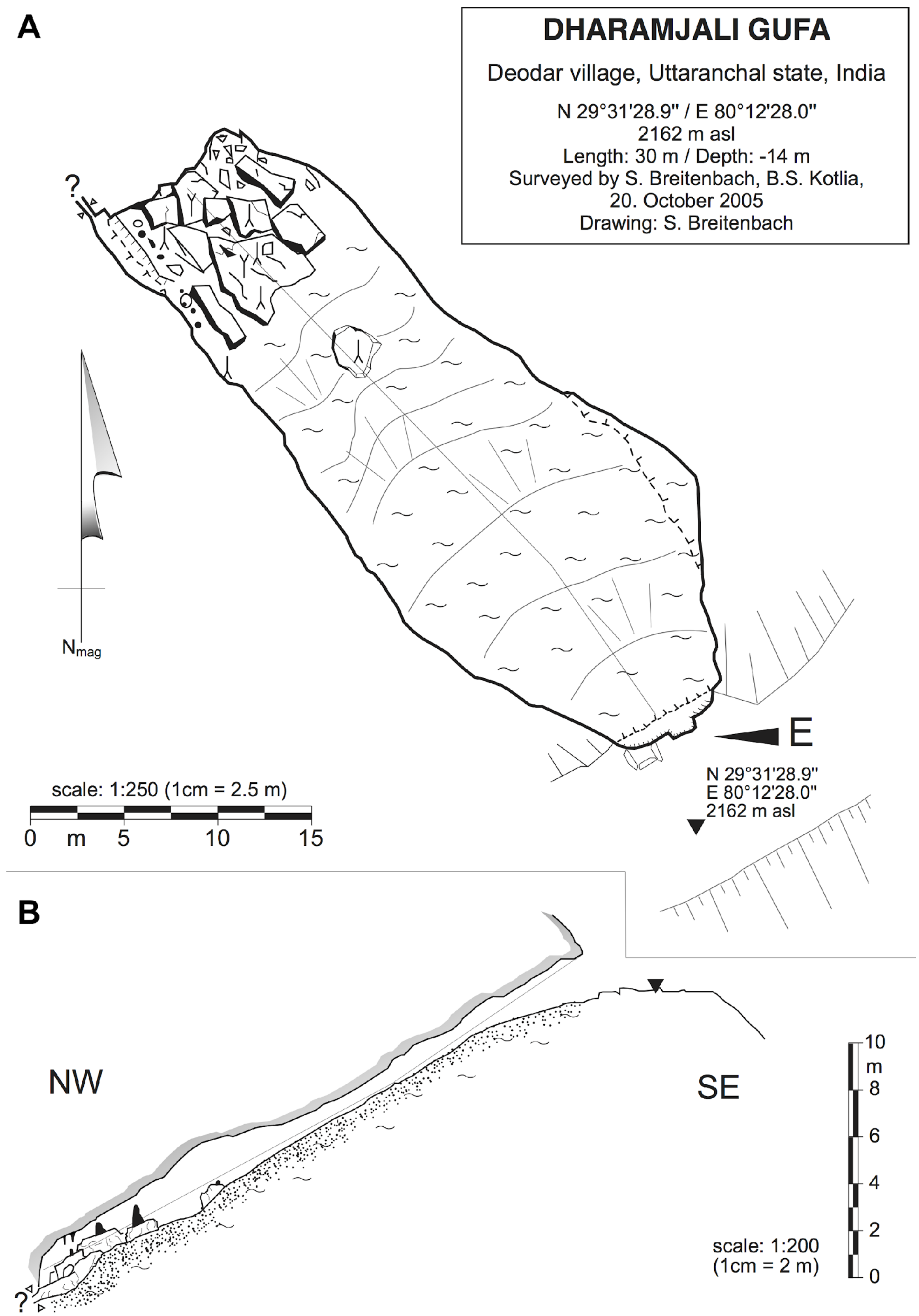

Fig. S10. Plan view and cross-section view of Dharamjali Cave from the 2005 survey (Breitenbach and Gebauer, 2013). Stalagmite DHAR-1 was obtained from the deepest part of the cave (length 30 m, depth 14 m).

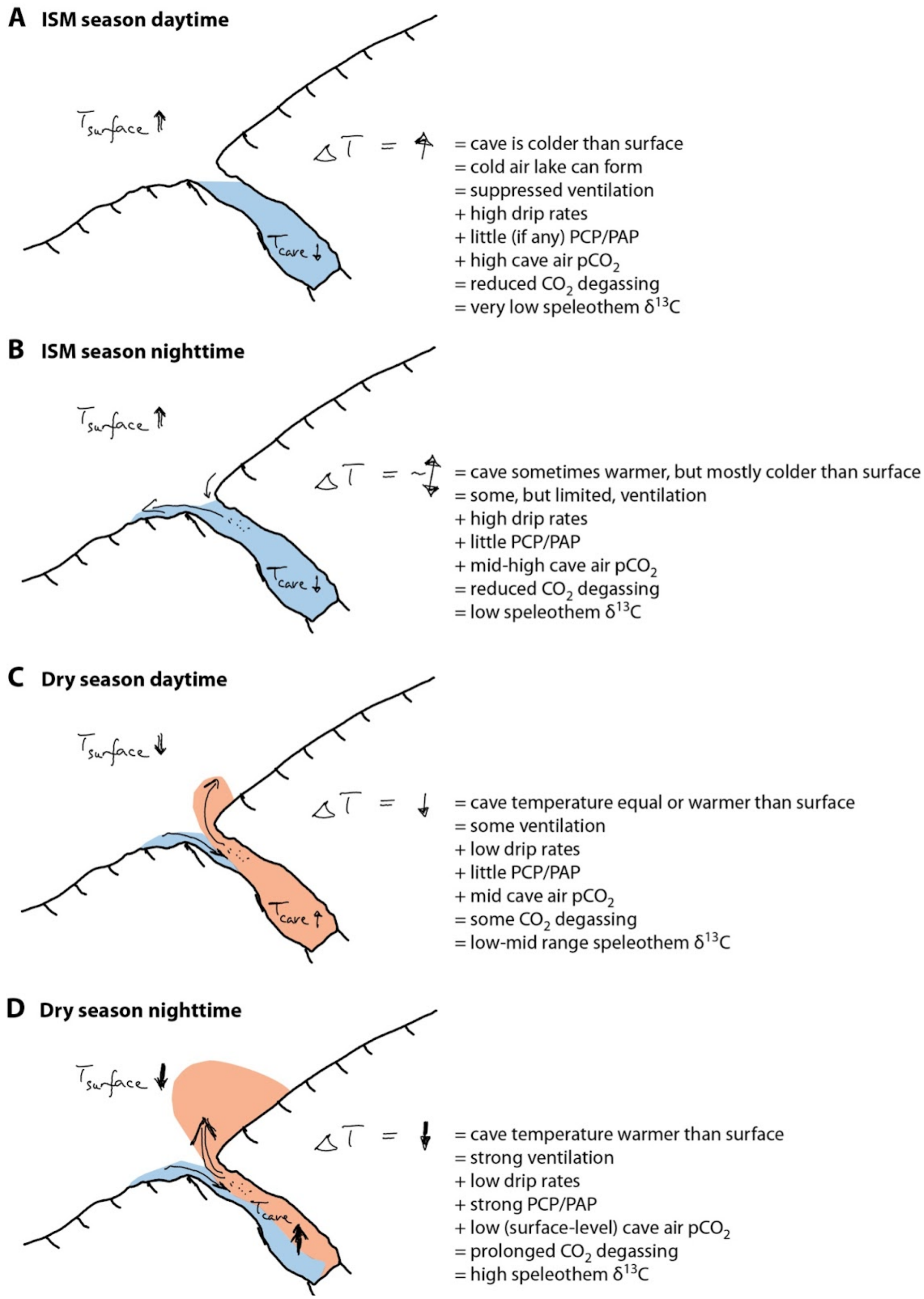

Fig. S11 Hypothetical scenarios of ventilation regimes at Dharamjali Cave. (a) colder-than-surface cave air temperatures during daytime suppress ventilation during the ISM season. **(b)** Ventilation remains suppressed during nighttime in the wet season, with only limited air exchange. **(c)** Ventilation is possible during winterly dry season daytime when surface air is cooler than cave air. **(d)** Ventilation is strongest during winterly dry season nights, when the cave air is significantly warmer than surface air. Prior carbonate/aragonite precipitation is enhanced during the dry season. Drip rates are highest during the ISM and post-ISM seasons **(a, b)**, whereas little water comes into the cave during the dry season **(c, d)**. Note: cave is not drawn to scale.

Table S1. Archives numbered in Figure S1.

Number	Record
1	Dharamjali speleothem (this study)
2	Khajuwala playa, Lunkaransar playa (Enzel et al., 1999), and Karsandi playa (Dixit et al., 2018),
3	Core 63KA (Staubwasser et al., 2003, Giesche et al., 2019)
4	West Canadian glaciers (Menounos et al., 2008)
5	Lake Titicaca (Tapia et al., 2003)
6	Peat bog (Jordan et al., 2017)
7	Lake Ledro (Magny et al., 2012)
8	Dante speleothem (Railsback et al., 2018)
9	Xianglong speleothem (Tan et al., 2018)
10	Heshang speleothem (Hu et al., 2008)
11	Shennong speleothem (Zhang et al., 2018)
12	South Rhody peatland (Booth et al., 2005)
13	Huascarán ice core (Davis and Thompson, 2006)
14	Laguna Cháltel (Ohlendorf et al., 2014)
15	Buca della Renella speleothem (Drysdale et al., 2006) and Corchia speleothem (Regattieri et al., 2014)
16	Skala Marion speleothem (Psomiadis et al., 2018)
17	Core S-21, S-86, S-87 (Stanley et al., 2003)
18	Lake Yoa (Kröpelin et al., 2008)
19	Mt. Kilimanjaro ice core (Thompson et al., 2002)
20	Soreq speleothem (Bar- Matthews and Ayalon, 2011)
21	Core GeoB 5836-2 (Arz et al., 2006)
22	Lake Van (Wick et al., 2003)
23	Gol-e-Zard speleothem (Carolin et al., 2019)
24	Core M5-422 (Cullen et al., 2000)
25	Core 723A, RC27-14, RC27-23, RC27-28 (Overpeck et al., 1996, Gupta et al., 2003), just west of here is Qunf speleothem showing no event (Fleitmann et al., 2003)
26	Kotla Dahar lake (Dixit et al., 2014)
27	Sahiya speleothem (Kathayat et al., 2017), Din Gad peat record (Phadtare, 2000), and Tso Moriri lake (Dutt et al., 2018)
28	Rara lake (Nakamura et al., 2016)
29	Lonar lake (Menzel et al., 2014, Prasad et al., 2020)
30	Mawmluh speleothem (Berkelhammer et al., 2012, Kathayat et al., 2018)
31	Hongyuan peat bog (Hong et al., 2003)
32	Dongge speleothem (Dykoski et al., 2005, Wang et al., 2005)
33	Shanbao speleothem (Shao et al., 2006)
34	Hunshandake Sandy lands (Yang et al., 2015)
35	KNI-51 speleothem (Denniston et al., 2013)

Table S2. U-series dates for DHAR-1, with highlighted depths denoting dates used in the age model. One date was selected per isochron (U15b, U6c, and U11d) based on the lowest ^{232}Th (and correspondingly lowest error). Three dates at the top were excluded from the age model because of possible dissolution in this section of the stalagmite (U17, U14, and U16), and three were excluded based on large spatial integration (U1, first test date with larger sample size) or large ^{232}Th errors (U13, U18).

Master depth (mm)	Lab code	^{238}U (ppb)	^{232}Th (pmol/g)	Corrected age (yr BP)	± 2σ error (yrs)
12.1	SJ17_U17	835.5	5.3	554.4	48.5
19.2	SH11_U14	45.3	35.7	-1169.8	3490.6
27	SJ18_U16	51.1	17.6	-228.8	1433.2
39.6	SH03_U8	1847.7	28.3	2554.2	70.3
48.5	SG34_U2	2976.3	7.5	2607.5	12.3
69.35	SH14_U7	3439.9	17.5	2748.0	23.9
74.5	SH04_U15a	3933.5	12.8	2777.1	15.4
74.5	SH13_U15b	3626.9	5.6	2769.1	9.5
74.5	SH22_U15c	3691.3	10.5	2772.9	14.0
74.5	SH18_U15d	3372.0	33.4	2743.6	44.7
79.75	SH05_U13	2749.4	56.0	2970.5	92.6
83.4	SJ19_U18	3344.8	20.2	2862.3	29.8
113.2	SH17_U12	3524.2	7.2	2998.8	10.8
147.6	SH09_U5	3731.1	7.1	3093.8	9.8
156.4	SH20_U4	3350.4	30.3	3151.2	40.7
192.6	SH19_U6a	5785.5	3.8	3517.3	5.4
192.6	SH12_U6b	5278.1	11.1	3516.1	11.9
192.6	SH01_U6c	4914.5	3.1	3498.7	5.4
192.6	SH07_U6d	4470.0	6.6	3506.2	9.4
206.6	SH02_U3	6056.9	3.2	3613.6	5.7
218.4	SH06_U9a	4914.7	12.6	3784.2	13.9
221.6	SG35_U1	4096.7	16.9	3667.0	21.7
234.7	SH10_U11a	4793.3	6.3	3914.1	9.1
234.7	SH21_U11b	4648.2	12.0	3929.6	13.5
234.7	SH15_U11c	4977.4	2.3	3952.0	7.7
234.7	SH08_U11d	4664.0	1.9	3968.9	8.1
244.3	SH16_U10a	3397.2	1.6	4142.3	7.1

Supplementary References for Figures & Tables

1. Meyer-Christoffer, A., Becker, A., Finger, P., Schneider, U., Ziese, M. Data from "GPCC Climatology Version 2018 at 0.25°: Monthly Land-Surface Precipitation Climatology for Every Month and the Total Year from Rain-Gauges built on GTS-based and Historical Data." GPCC at DWD. Available at https://doi.org/ 10.5676/DWD_GPCC/CLIM_M_V2018_025, Deposited 2018.
2. Staubwasser, M., Sirocko, F., Grootes, P. M., Segl, M. Climate change at the 4.2 ka BP termination of the Indus valley civilization and Holocene south Asian monsoon variability. *Geophys. Res. Lett.*, **30** (2003).
3. Giesche, A., Staubwasser, M., Petrie, C. A., Hodell, D. A. Indian winter and summer monsoon strength over the 4.2 ka BP event in foraminifer isotope records from the Indus River delta in the Arabian Sea. *Clim. Past*, **15**, 73-90, (2019).
4. Enzel, Y. et al. High-resolution Holocene environmental changes in the Thar Desert, northwestern India. *Science*, **284**, 125-128 (1999).
5. Dixit, Y. et al. Intensified summer monsoon and the urbanization of Indus Civilization in northwest India. *Sci. Rep.*, **8**, 1-8 (2018).
6. Menounos, B. et al. Western Canadian glaciers advance in concert with climate change circa 4.2 ka. *Geophys. Res. Lett.*, **35** (2008).
7. Tapia, P. M., Fritz, S. C., Baker, P. A., Seltzer, G. O., Dunbar, R. B. A Late Quaternary diatom record of tropical climatic history from Lake Titicaca (Peru and Bolivia). *Palaeogeogr. Palaeoclimatol. Palaeoecol.*, **194**, 139-164 (2003).
8. Jordan, S. F. et al. Mid-Holocene climate change and landscape formation in Ireland: Evidence from a geochemical investigation of a coastal peat bog. *Org. Geochem.*, **109**, 67-76 (2017).
9. Magny, M. et al. Holocene palaeohydrological changes in the northern Mediterranean borderlands as reflected by the lake-level record of Lake Ledro, northeastern Italy. *Quat. Res.*, **77**, 382-396 (2012).
10. Railsback, L. B. et al. The timing, two-pulsed nature, and variable climatic expression of the 4.2 ka event: A review and new high-resolution stalagmite data from Namibia. *Quat. Sci. Rev.*, **186**, 78-90 (2018).
11. Tan, L. et al. Centennial-to decadal-scale monsoon precipitation variations in the upper Hanjiang River region, China over the past 6650 years. *Earth Planet. Sci. Lett.*, **482**, 580-590 (2018).
12. Hu, C. et al. Quantification of Holocene Asian monsoon rainfall from spatially separated cave records. *Earth Planet. Sci. Lett.*, **266**, 221-232 (2008).
13. Zhang, H. et al. Hydroclimatic variations in southeastern China during the 4.2 ka event reflected by stalagmite records. *Clim. Past*, **14**, 1805-1817 (2018).
14. Booth, R. K. et al. A severe centennial-scale drought in midcontinental North America 4200 years ago and apparent global linkages. *Holocene*, **15**, 321-328 (2005).
15. Davis, M. E., Thompson, L. G. An Andean ice-core record of a Middle Holocene mega-drought in North Africa and Asia. *Ann. Glaciol.*, **43**, 34-41 (2006).
16. Ohlendorf, C. et al. Late Holocene hydrology inferred from lacustrine sediments of Laguna Cháltel (southeastern Argentina). *Palaeogeogr. Palaeoclimatol. Palaeoecol.*, **411**, 229-248 (2014).
17. Drysdale, R. et al. Late Holocene drought responsible for the collapse of Old World civilizations is recorded in an Italian cave flowstone. *Geology*, **34**, 101-104 (2006).
18. Regattieri, E. et al. Lateglacial to Holocene trace element record (Ba, Mg, Sr) from Corchia Cave (Apuan Alps, central Italy): paleoenvironmental implications. *J. Quat. Sci.*, **29**, 381-392 (2014).
19. Psomiadis, D., Dotsika, E., Albanakis, K., Ghaleb, B., Hillaire-Marcel, C. Speleothem record of climatic changes in the northern Aegean region (Greece) from the Bronze Age to the collapse of the Roman Empire. *Palaeogeogr. Palaeoclimatol. Palaeoecol.*, **489**, 272-283 (2018).
20. Stanley, J. D., Krom, M. D., Cliff, R. A., Woodward, J. C. Short contribution: Nile flow failure at the end of the Old Kingdom, Egypt: strontium isotopic and petrologic evidence. *Geoarchaeology*, **18**, 395-402 (2003).
21. Kröpelin, S. et al. Climate-driven ecosystem succession in the Sahara: the past 6000 years. *Science*, **320**, 765-768 (2008).
22. Thompson, L. G. et al. Kilimanjaro ice core records: evidence of Holocene climate change in tropical Africa. *Science*, **298**, 589-593 (2002).
23. Bar-Matthews, M., Ayalon, A. Mid-Holocene climate variations revealed by high-resolution speleothem records from Soreq Cave, Israel and their correlation with cultural changes. *Holocene*, **21**, 163-171 (2011).
24. Arz, H. W., Lamy, F., Pätzold, J. A pronounced dry event recorded around 4.2 ka in brine sediments from the northern Red Sea. *Quat. Res.*, **66**, 432-441 (2006).
25. Wick, L., Lemcke, G., Sturm, M. Evidence of Lateglacial and Holocene climatic change and human impact in eastern Anatolia: high-resolution pollen, charcoal, isotopic and geochemical records from the laminated sediments of Lake Van, Turkey. *Holocene*, **13**, 665-675 (2003).
26. Carolin, S. A. et al. Precise timing of abrupt increase in dust activity in the Middle East coincident with 4.2 ka social change. *Proc. Natl. Acad. Sci. U.S.A.*, **116**, 67-72 (2019).
27. Cullen, H. M. et al. Climate change and the collapse of the Akkadian empire: Evidence from the deep sea. *Geology*, **28**, 379-382 (2000).

28. Overpeck, J., Anderson, D., Trumbore, S., Prell, W. The southwest Indian Monsoon over the last 18000 years. *Clim. Dyn.*, **12**, 213-225 (1996).
29. Gupta, A. K., Anderson, D. M., Overpeck, J. T. Abrupt changes in the Asian southwest monsoon during the Holocene and their links to the North Atlantic Ocean. *Nature*, **421**, 354-357 (2003).
30. Fleitmann, D. et al. Holocene forcing of the Indian monsoon recorded in a stalagmite from southern Oman. *Science*, **300**, 1737-1739 (2003).
31. Dixit, Y., Hodell, D. A., Petrie, C. A. Abrupt weakening of the summer monsoon in northwest India~ 4100 yr ago. *Geology*, **42**, 339-342 (2014).
32. Kathayat, G. et al. The Indian monsoon variability and civilization changes in the Indian subcontinent. *Sci. Adv.*, **3**, e1701296 (2017).
33. Phadtare, N. R. Sharp decrease in summer monsoon strength 4000–3500 cal yr BP in the Central Higher Himalaya of India based on pollen evidence from alpine peat. *Quat. Res.*, **53**, 122-129 (2000).
34. Dutt, S., Gupta, A. K., Wünnemann, B., Yan, D. A long arid interlude in the Indian summer monsoon during~ 4,350 to 3,450 cal. yr BP contemporaneous to displacement of the Indus valley civilization. *Quat. Int.*, **482**, 83-92 (2018).
35. Nakamura, A. et al. Weak monsoon event at 4.2 ka recorded in sediment from Lake Rara, Himalayas. *Quat. Int.*, **397**, 349-359 (2016).
36. Menzel, P. et al. Linking Holocene drying trends from Lonar Lake in monsoonal central India to North Atlantic cooling events. *Palaeogeogr. Palaeoclimatol. Palaeoecol.*, **410**, 164-178 (2014).
37. Prasad, S. et al. Holocene climate forcings and lacustrine regime shifts in the Indian summer monsoon realm. *Earth Surf. Process. Landf.*, **45**, 3842-3853 (2020).
38. Berkelhammer, M. et al. An abrupt shift in the Indian monsoon 4000 years ago. *Geophys. Monogr. Ser.*, **198**, 75-87 (2012).
39. Kathayat, G. et al. Evaluating the timing and structure of the 4.2 ka event in the Indian summer monsoon domain from an annually resolved speleothem record from Northeast India. *Clim. Past*, **14**, 1869-1879, (2018).
40. Hong, B. et al. Carbon isotopic composition of the *Carex mulieensis* remain of the Hongyuan peat bog in the eastern Tibetan Plateau and the Indian Ocean summer monsoon variation in the Holocene. *Bull. Mineral. Petrol. Geochem.*, **2**, 99-103 (2003).
41. Dykoski, C. A. et al. A high-resolution, absolute-dated Holocene and deglacial Asian monsoon record from Dongge Cave, China. *Earth Planet. Sci. Lett.*, **233**, 71-86 (2005).
42. Wang, Y. et al. The Holocene Asian monsoon: links to solar changes and North Atlantic climate. *Science*, **308**, 854-857 (2005).
43. Shao, X. et al. Long-term trend and abrupt events of the Holocene Asian monsoon inferred from a stalagmite $\delta^{18}O$ record from Shennongjia in Central China. *Sci. Bull.*, **51**, 221-228 (2006).
44. Yang, X. et al. Groundwater sapping as the cause of irreversible desertification of Hunshandake Sandy Lands, Inner Mongolia, northern China. *Proc. Natl. Acad. Sci. U.S.A.*, **112**, 702-706 (2015).
45. Denniston, R. F. et al. A Stalagmite record of Holocene Indonesian–Australian summer monsoon variability from the Australian tropics. *Quat. Sci. Rev.*, **78**, 155-168 (2013).
46. Bowen, G. J., Revenaugh, J. Interpolating the isotopic composition of modern meteoric precipitation. *Water Resour. Res.* 39, 1299 (2003).
47. Palmer, W. C., Havens, A. V. A Graphical technique for determining evapotranspiration by the Thornthwaite method. *Mon. Weather Rev.* **86**, 123-128 (1958).
48. Rawal, R. S., Pangtey, Y. P. S. Distribution and phenology of climbers of Kumaun in Central Himalaya, India. *Vegetatio*, ***97***, 77-87 (1991).
49. Sanwal, J. et al. Climatic variability in Central Indian Himalaya during the last~ 1800 years: Evidence from a high resolution speleothem record. *Quat. Int.*, **304**, 183-192 (2013).
50. Berkelhammer, M. et al. An abrupt shift in the Indian monsoon 4000 years ago. *Geophys. Monogr. Ser.* **198**, 75–87 (2012).
51. Breitenbach, S. F. M. et al. COnstructing Proxy Records from Age models (COPRA). *Clim. Past* **8**, 1765-1779 (2012).
52. Kotlia, B. S., Singh, A. K., Joshi, L. M., Bisht, K. Precipitation variability over Northwest Himalaya from ~4.0 to 1.9 ka BP with likely impact on civilization in the foreland areas. *J. Asian Earth Sci.*, 162, 148-159 (2018).

53. Wassenburg, J. A. et al., Determination of aragonite trace element partition coefficients from speleothem calcite-aragonite transitions. *Geochim. Cosmochim. Acta* **190**, 347-367 (2016).
54. Jamieson, J. R. A. et al. Intra- and inter-annual uranium concentration variability in a Belizean stalagmite controlled by prior aragonite precipitation: a new tool for reconstructing hydro-climate using aragonitic speleothems. *Geochim. Cosmochim. Acta* **190**, 332-346 (2016).
55. Breitenbach, S. F. M., Gebauer, D. Resources on the Speleology of Uttarakhand state, India. *Berliner Höhlenkundliche Berichte* **50**, 199 pages (2013).

The following data is uploaded to the publicly available Apollo online repository hosted by the University of Cambridge (https://doi.org/10.17863/CAM.95036):

Table X1. (stable isotope data: $\delta^{18}O$, $\delta^{13}C$, $\delta^{44}Ca$)
Table X2. (XRF data)
Table X3. (LA-ICP-MS data)
Table X4. (DHAR 2006 cave drip water measurements)
Table X5. (U-series dates)